Chinese Journal of Mechanical Engineering

ORIGINAL ARTICLE

Open Access

Optimal Design of the Modular Joint Drive Train for Enhancing Cobot Load Capacity and Dynamic Performance

Peng Li[1,2,3], Zhenguo Nie[1,2,3*], Zihao Li[1,2,3] and Xinjun Liu[1,2,3*]

Abstract

Automation advancements prompts the extensive integration of collaborative robot (cobot) across a range of industries. Compared to the commonly used design approach of increasing the payload-to-weight ratio of cobot to enhance load capacity, equal attention should be paid to the dynamic response characteristics of cobot during the design process to make the cobot more flexible. In this paper, a new method for designing the drive train parameters of cobot is proposed. Firstly, based on the analysis of factors influencing the load capacity and dynamic response characteristics, design criteria for both aspects are established for cobot with all optimization design criteria normalized within the design domain. Secondly, with the cobot in the horizontal pose, the motor design scheme is discretized and it takes the joint motor diameter and gearbox speed ratio as optimization design variables. Finally, all the discrete values of the optimization objectives are obtained through the enumeration method and the Pareto front is used to select the optimal solution through multi-objective optimization. Base on the cobot design method proposed in this paper, a six-axis cobot is designed and compared with the commercial cobot. The result shows that the load capacity of the designed cobot in this paper reaches 8.4 kg, surpassing the 5 kg load capacity commercial cobot which is used as a benchmark. The minimum resonance frequency of the joints is 42.70 Hz.

Keywords Multi-objective optimization, Modular joint drive train design, Load capacity, Dynamic response performance

1 Introduction

The collaborative robot (cobot) represents a novel category of robots specifically designed to physically interact with humans in shared environments, eliminating the traditional barriers or protective cages found in conventional robotics systems [1–3]. Possessing characteristics such as lightweight design, enhanced safety features, and simplified mechanisms for seamless human interaction, cobot find widespread applications in processing, assembly, surgery, and rehabilitation. Comprising lightweight linkages and modular joints, these components serve as the driving force for the cobot's movements. Modular joints, as the driving components of cobot, have been extensively studied by numerous scholars due to their ability to achieve the unique performance of cobot through their drive train design.

Unlike the high load capacity characteristic of industrial robots, collaborative robots have a relatively lower load capacity, which limits their scope of application. Reducing the weight of the cobot itself or increasing the load-to-self-mass ratio is an effective method to enhance the cobot's load capacity. In this regard, many scholars

*Correspondence:
Zhenguo Nie
zhenguonie@tsinghua.edu.cn
Xinjun Liu
xinjunliu@mail.tsinghua.edu.cn
[1] Department of Mechanical Engineering, Tsinghua University, Beijing 100084, China
[2] State Key Laboratory of Tribology in Advanced Equipment, Tsinghua University, Beijing 100084, China
[3] Beijing Key Lab of Precision/Ultra-precision Manufacturing Equipments and Control, Tsinghua University, Beijing 100084, China

have conducted relevant work. An optimization objective that includes all the mass of motors and reducers is proposed by Zhou et al. [4–6], and the motors and reducers are selected by minimizing the objective. Yin et al. research the hybrid structure cobot links and the drive train regression design to achieve the lightweight of the cobot [7–9]. With the development of cobot, more performance is concerned. A multi-objective optimization function is proposed to reduce the mass and expand the workspace of the cobot [10]. The workspace and the mass of the cobot, including motors, gearboxes, and links, are combined with the scalarization method. Different from Ref. [10], Kawaharazuka et al. replace the workspace with manipulability, increasing flexibility while reducing the cobot mass [11]. The motor's mass, the reducer's mass, and the reducer's cost are added to the objective function to design the drive train with the scalarization method of multi-objective [12]. Padilla-Garcia et al. combine the total mass, tracking error, and the consumed energy to construct the optimal index, which is used to obtain comprehensive performance by configuring different motors [13]. The tracking error, manipulability, and consumed energy are optimized by selecting the motors and reducers [14].

Recently, there has been an increased focus on dynamic characteristics, given that a high dynamic response is not only effective in suppressing vibrations but also crucial for enhancing cobot compliance. This enhancement makes cobot safer for interaction with the environment and facilitates easier direct teaching and cooperation [15]. Du et al. conducted optimization on manipulator geometrical parameters and reducer selection to maximize fundamental frequency and payload-to-self-mass ratio [16]. The design objective is a two-link system, where frequency improvement is considered by accounting for only the reducer's stiffness and the manipulator's weight.

The servo control variables of robots are generally the torque, position, or velocity of the motors. The dynamic performance of each joint is affected not only by output inertia and reducer stiffness but also by motor axis inertia. Hence, it is imperative to adopt a more comprehensive design approach for the joint drive train to enhance cobot dynamic performance. Additionally, the cobot's load capacity, a critical indicator, must be taken into account in the design process—a factor frequently overlooked by other designers.

In this study, optimization functions for both the dynamic response performance and load capacity of cobot are concurrently developed. The Pareto front is employed to select the optimal joint drive chain design, ensuring the overall performance of the cobot is maximized. To validate the effectiveness of the design method, a case study is conducted using a commercial collaborative cobot with a 5-kilogram payload as the benchmark. The results indicate that this design method can simultaneously optimize the dynamic response performance and load capacity of cobot, achieving optimal performance.

This paper is organized as follows: Section 2 analyzes the drive train structure, encompassing the cobot and the modular joint. The dynamics of the joint are also examined in this section. Section 3 covers the motor's design process, used for calculating the motor mass and rotor inertia. The optimization objective and design process are presented in Section 5, and a design example is implemented to illustrate the validity of the design method. Finally, Section 5 provides the conclusion of the work.

2 Drive Train Analysis of Modular Joint

2.1 Cobot Structure Analysis

Figure 1 displays the commonly used types of cobot: six-axis and seven-axis. In the seven-axis cobot, it is typical for the three joints near the base to form a spherical pair by inter-secting axes at a point, which is also observed in the terminal three joints, as depicted in Figure 1(a).

The six-axis cobot can generally be classified into two categories, without considering the bias between the joints. In the first category, joints 3 and 4 form the elbow of the cobot, with the axes of these two joints being vertical, as illustrated in Figure 1(b). The second category features one joint forming the elbow, while the fourth joint is positioned near the end effector, as shown in Figure 1(c).

The seven-axis cobot stands out for its high flexibility, making it suitable for obstacle avoidance. Conversely, the six-axis cobot exhibits higher stiffness and precision, making it more suitable for industrial applications [17]. The fundamental units consist of modular joints and lightweight thin-walled links, with the modular joint serving as the actuator that significantly influences the dynamic performance of the cobot [18–20]. Due to the typical structure and greater applicability of six-axis

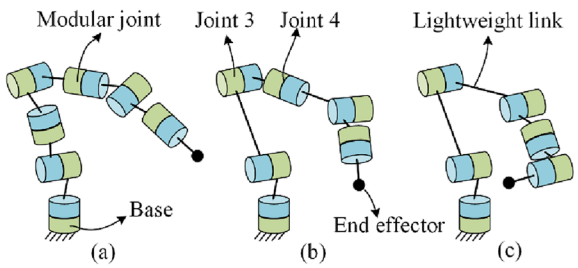

Figure 1 The configuration of cobot: (**a**) Configuration of the seven-axis cobot, (**b**) Six-axis cobot with two parallel axis configuration, (**c**) Six-axis cobot with three parallel axis configuration

collaborative robots, the analysis and design are conducted focusing on the joints of the six axes.

2.2 Modular Joint Structure Analysis

Figure 2 depicts a typical modular joint, serving as the design example in this study. The components are conventional, with the exception of the torque sensor, enhancing torque measurement accuracy. Typically, a harmonic reducer is employed, capitalizing on its features of a substantial reduction ratio and low mass to enhance joint integration [21].

The torque sensor is positioned on the reducer's output port, and the motor rotor is connected to the reducer's wave-generator through a hollow shaft. A brake near the motor can secure the hollow shaft to bring the motor to a stop. The encoder gauges the position of the motor or the output flange of the joint. Moreover, two encoders are configured to measure position information from both the motor and output port. The driver oversees motor movement, transmitting information through the bus to the controller.

2.3 Modular Joint Dynamic Analysis

The cobot is constructed with modular joints and lightweight links in a serial configuration. The output torque of the joint can be computed using Eqs. (1) and (2). This torque comprises inertial torque, Coriolis torque, gravity torque, damping torque, and external torque. The damping torque is the aggregate of viscous friction torque and Coulomb friction torque [22].

$$\boldsymbol{\tau} = \boldsymbol{M}(\boldsymbol{q})\ddot{\boldsymbol{q}} + \boldsymbol{C}(\boldsymbol{q},\dot{\boldsymbol{q}})\dot{\boldsymbol{q}} + \boldsymbol{g}(\boldsymbol{q}) + \boldsymbol{\tau}_f + \boldsymbol{\tau}_{ext}, \tag{1}$$

$$\boldsymbol{\tau}_f = \boldsymbol{D}\cdot\boldsymbol{q} + \boldsymbol{\mu}\cdot\operatorname{sgn}(\boldsymbol{q}). \tag{2}$$

In the equations, $\boldsymbol{\tau} \in \mathbb{R}^n$ represents the vector of joint output torque, $\boldsymbol{M}(\boldsymbol{q}) \in \mathbb{R}^{n\times n}$ is the symmetric and positive-definite inertia matrix, $\boldsymbol{C}(\boldsymbol{q},\dot{\boldsymbol{q}})\dot{\boldsymbol{q}} \in \mathbb{R}^n$ denotes the centripetal and Coriolis vector, $\boldsymbol{g}(\boldsymbol{q}) \in \mathbb{R}^n$ is the gravity vector, $\boldsymbol{\tau}_f \in \mathbb{R}^n$ signifies the damping vector, $\boldsymbol{\tau}_{ext} \in \mathbb{R}^n$ is the torque vector generated by the external forces and moments, $\boldsymbol{D} \in \mathbb{R}^n$ is the viscous friction torque coefficient vector, and $\boldsymbol{\mu} \in \mathbb{R}^n$ is the Coulomb friction torque coefficient vector. $\boldsymbol{q} \in \mathbb{R}^n$, $\dot{\boldsymbol{q}} \in \mathbb{R}^n$, $\ddot{\boldsymbol{q}} \in \mathbb{R}^n$ represent position, velocity and acceleration vector of the joints. Superscript 'n' denotes the number of joints. The external forces and speeds can be transformed into joint space using the inverse Jacobian matrix in Eqs. (3) and (4):

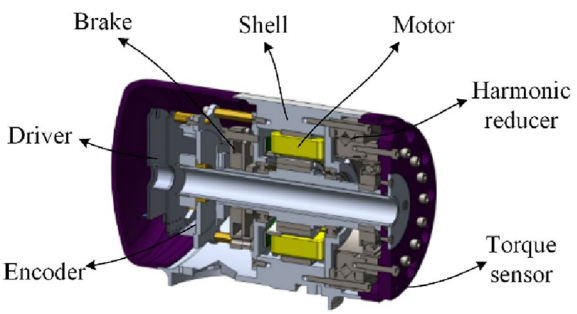

Figure 2 Section view of a typical modular joint

$$\boldsymbol{F} = \boldsymbol{J}\boldsymbol{\tau}_{ext}, \tag{3}$$

$$\dot{\boldsymbol{x}} = \boldsymbol{J}\dot{\boldsymbol{q}}. \tag{4}$$

In the equations, $\boldsymbol{J} \in \mathbb{R}^{n\times 6}$ represents the Jacobian matrix, $\boldsymbol{F} \in \mathbb{R}^{6\times 1}$ is the vector of external force and moment, and $\dot{\boldsymbol{x}} \in \mathbb{R}^{6\times 1}$ is the vector of endpoint speed.

The load and speed of the joint are crucial factors in selecting the harmonic reducer, ensuring compliance with the constraints specified in Eqs. (5) to (7). τ represents the reducer output torque, and τ_{peak} is the maximum output torque of the reducer. $\dot{q}$ denotes the joint speed, and $\dot{q}_{peak}$ is the maximum output speed of the reducer. τ_{rrms} stands for the maximum mean torque of the reducer, and the joint mean torque τ_{jrms} must be less than this value.

$$\max|\tau| \le \tau_{peak}, \tag{5}$$

$$\max|\dot{q}| \le \dot{q}_{peak}, \tag{6}$$

$$\tau_{jrms} = \sqrt{(1/t)\int_0^t \tau_j^2 \mathrm{d}t} \le \tau_{rrms}. \tag{7}$$

The joint motor shaft rotational inertia $J_{m,k}$ is expressed in Eq. (8), where $J_{rotor,k}$ denotes the motor rotor rotational inertia, and $J_{parts,k}$ is the rotational inertia of various components, encompassing the wave-generator, CNC-machined aluminum alloy shaft, bearing rotation, and encoder rotation. Given the low density of the rotating component of the brake, its rotational inertia can be considered negligible. The variable subscript 'k' refers to the k-th joint starting from the cobot base, and the subsequent descriptions of variables follow the same convention.

$$J_{m,k} = J_{rotor,k} + J_{parts,k}. \tag{8}$$

The transmission mechanism of the harmonic reducer involves the wave-generator pressing against the gear of the flexspline on the circular spline. The flexspline should be designed to be thin and soft compared to the gearbox. This design imparts softness to the harmonic reducer, and its flexibility should be taken into account in the dynamic modeling and control of the modular joint.

Illustrated in Figure 3, $\tau_{m,k}$ represents the motor torque applied by the stator to the rotor. $b_{m,k}$ is the damping coefficient of the motor shaft, influenced by the motor bearing and the harmonic reducer wave generator. K_k denotes the stiffness of the joint, which is the reducer stiffness if the joint lacks a torque sensor. $b_{l,k}$ is the damping coefficient on the joint output side, and $J_{l,k}$ is the inertia of the joint output side.

The mathematical expressions are presented in Eqs. (9) to (12). Here θ_k represents the position of the motor, while $\ddot{\theta}_k$ and $\dot{\theta}_k$ denote the acceleration and velocity of the motor, respectively. $\tau_{mo,k}$ is the effective torque transmitted by the reducer from the motor, and N_k is the reduction ratio of the reducer $\tau_{l,k}$ and $\tau_{ext,k}$ represent the torque applied to the link by the reducer and the external force, respectively. q_k signifies the position of the link, while $\ddot{q}_k$ and $\dot{q}_k$ are the acceleration and velocity of the link, respectively.

$$\tau_{m,k} = J_{m,k}\ddot{\theta}_k + b_{m,k}\dot{\theta}_k + \tau_{mo,k}, \tag{9}$$

$$K_k(\theta_k/N_k - q_k) = \tau_{l,k}, \tag{10}$$

$$N_k \cdot \tau_{mo,k} = \tau_{l,k}, \tag{11}$$

$$\tau_{l,k} = J_{l,k}\ddot{q}_k + b_{l,k}\dot{q}_k + \tau_{ext,k}. \tag{12}$$

Since the joint control primarily targets the motor, the transfer function from torque to motor velocity is derived, as presented in Eqs. (13) to (15). In this context, external forces act as disturbances, and the damp torque is negligible, allowing it to be disregarded.

$$\frac{\dot{\theta}_k(s)}{\tau_{m,k}(s)} = \frac{sN_k^2(B_k + K_k)}{N_k^2 A_k B_k + K_k(N_k^2 A_k + B_k)}, \tag{13}$$

$$A_k = J_{m,k}s^2 + b_{m,k}s, \tag{14}$$

$$B_k = J_{l,k}s^2 + b_{l,k}s. \tag{15}$$

The two-inertia system exhibits resonance frequency and anti-resonance frequency, depicted in Eqs. (16) and (17), especially when the damping coefficient is small.

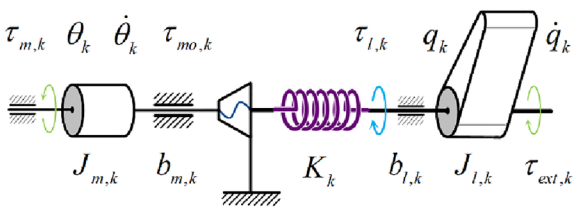

Figure 3 Dynamics model diagram of modular joint

The resonance frequency indicates that the joint experiences intense vibration, while the anti-resonance frequency implies that the motor cannot effectively execute instructions from the driver. Consequently, the joint may become uncontrollable at these specific frequencies.

$$\omega_{NTR,k} = \sqrt{\frac{K_k(J_{l,k} + N_k^2 J_{m,k})}{N_k^2 J_{m,k} J_{l,k}}}, \tag{16}$$

$$\omega_{ARF,k} = \sqrt{\frac{K_k}{J_{l,k}}}. \tag{17}$$

The transfer function exhibits zeros and poles at $\omega_{ARF,k}$ and $\omega_{NTF,k}$. Given that a higher resonance frequency allows for greater control bandwidth, thereby enhancing dynamic performance [23], one of the design objectives for the cobot is to increase the resonance frequency.

3 Motor Design Process

Considering that the motor's mass impacts the inertia of other joints and the cobot's lifting capacity, and the shaft inertia influences the resonance frequency, the motor design process is thoroughly examined to identify the optimal design scheme. This section primarily focuses on the motor design process concerning mass and rotor inertia.

3.1 Constraints of Torque and Speed

The motor's rated torque is contingent on the reducer, with a larger reduction ratio requiring less torque. Eqs. (18) and (19) represent the peak load and the rated load, respectively, where η_k is the reducer efficiency at 55 ℃ and 2000 r/min rated input speed.

$$\left\|\tau_{m,k}\right\|_\infty = \max\left|J_{m,k}N_k\ddot{q}_k + b_{m,k}N_k\dot{q}_k + \frac{\tau_{l,k}}{N_k \cdot \eta_k}\right| \le \tau_{mp,k}, \tag{18}$$

$$\left\|\tau_{m,k}\right\| = \sqrt{\frac{1}{t}\int_0^t \tau_{m,k}^2 \mathrm{d}t} = \tau_{mc,k}. \tag{19}$$

The motor speed must adhere to the constraint outlined in Eq. (20) to ensure that the joint speed is adequate.

$$\dot{\theta}_k = N_k\dot{q}_k \le \dot{\theta}_{rated,k}. \tag{20}$$

3.2 Constrains of Power Supply

The joint functions as a servo system configured with a driver, which propels the motor in accordance with commands from the controller. Since the driver operates in space vector pulse width modulation (SVPWM) mode [24, 25] the motor voltage must adhere to Eq.

(21). Here, V_{rated} represents the bus voltage, the V_{lost} is the lost voltage on the driver, and u_{ph} and u_{phmax} denote the phase voltage and the maximum phase voltage, respectively.

$$u_{ph} \le u_{phmax} = \frac{\sqrt{3}}{3}(V_{rated} - V_{lost}). \tag{21}$$

The current at the operating point must conform to Eq. (22), where $i_{q,k}$ represents the cross axis, and $I_{rated,k}$ is the root mean square (RMS) of the motor's rated current.

$$i_{q,k} = \sqrt{2} I_{rated,k}. \tag{22}$$

3.3 Calculation of Motor Mass and Rotor Inertia

Motor design encompasses various parameters, including both dimensional and electromagnetic aspects. In this paper, the design work primarily focuses on the motor's dimensions to calculate mass and inertia. Illustrated in Figure 4, the motor consists of the stator steel, armature, rotor, magnets, and yokes, all assembled together. The rotor's inner and outer diameters are denoted by $d_{1,k}$ and $d_{2,k}$ respectively, while the stator's inner and outer diameters are $D_{1,k}$ and $D_{2,k}$. The parameters $t_{1,k}$, $t_{2,k}$, $t_{3,k}$, $t_{4,k}$, $t_{5,k}$, $t_{6,k}$, they are teeth height, pole boot height, teeth width, slot depth, the yoke width of the stator, and the width of the notch, respectively. The magnet steel width is $b_{mg,k}$, and its thickness is $l_{m,k}$. The length of the air gap is denoted by $l_{g,k}$, and the stator's thickness is l_k, representing the depth in the vertical straight direction on the paper. The motor shaft is designed to be hollow to facilitate routing and reduce mass. The variable in motor design is the motor length, with other parameters changing correspondingly based on the motor length.

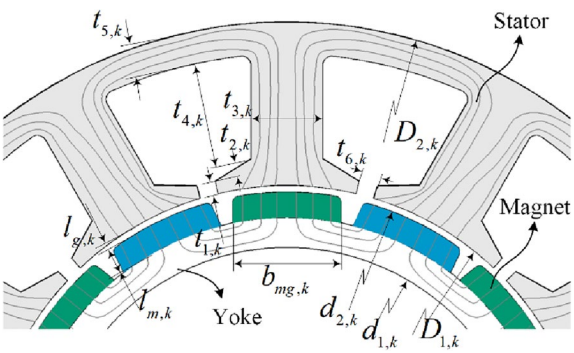

Figure 4 Motor dimension design illustration

Eq. (23) can be used to calculate the width of the magnet $b_{mg,k}$, where $t_{s,k}$ is the polar arc coefficient, and p_k represents the number of polar pairs.

$$b_{mg,k} = \frac{\pi d_{2,k}}{2p_k} t_{s,k}. \tag{23}$$

The electromagnetic parameters are computed as follows:

$$k_{l,k} = 1 - \frac{7p_k/30 - 0.5}{100}, \tag{24}$$

$$\kappa_k = \frac{(t_{6,k}/l_{g,k})^2}{4.4 + 0.75(t_{6,k}/l_{g,k})}, \tag{25}$$

$$k_{c,k} = \frac{\pi D_{1,k}}{\pi D_{1,k} - 2p_k \kappa_k l_{g.k}}, \tag{26}$$

$$t_{se,k} = \frac{\pi(2l_{g,k}k_{c,k} + d_{2,k})}{z_k}, \tag{27}$$

$$\phi_{l,k} = \frac{\frac{B_{r,k}l_{m,k}}{\mu_r} + \frac{B_{dw,k}L_{dw,k}}{\mu_{rdw,k}} + \frac{B_{stl,k}L_{stl.k}}{\mu_{rstl,k}}}{\frac{l_{m,k}}{\mu_r b_{mg,k}} + \frac{l_{g,k}k_{c,k}}{t_{se,k}}}, \tag{28}$$

$$B_{g,k} = \frac{\phi_{l,k}}{t_{se,k}}, \tag{29}$$

where $k_{l,k}$ is the magnetic leakage factor, $k_{c,k}$ is the Carter factor, $t_{se,k}$ is the equivalent air gap length, $B_{g,k}$ is the air gap magnetic density, $\phi_{l,k}$ and κ_k are the intermediate variables, z_k is the teeth number, $B_{dw,k}$ and $B_{stl,k}$ are magnetic flux density of the stator steel and the rotor yoke, $L_{dw,k}$ and $L_{stl,k}$ are the length of the magnet path, $\mu_{rdw,k}$, $\mu_{rstl,k}$, and μ_r are the relative permeability of stator steel, rotor yoke steel and the magnet steel. The length of the motor can be calculated using Eq. (30), and the area of the slot is given by Eq. (32):

$$l_k = \pi W_{rated,k}/(6i_q n_{rated,k} p_k N_{ph,k} k_{w,k} t_{se,k} B_{g,k}), \tag{30}$$

$$S_{slot,k} = \frac{\pi t_{4,k}(D_{1,k} + 2t_{1,k} + 2t_{2,k} + t_{4,k})^2}{z_k} - t_{3,k}t_{4,k}, \tag{31}$$

$$l_{R,k} = 6N_{ph,k}(l_k + t_{3,k}), \tag{32}$$

where $W_{rated,k}$ is the rated power of the motor, $n_{rated,k}$ is the motor rated speed, $N_{ph,k}$ is the phase turns number, $k_{w,k}$ is the winding factor, $S_{slot,k}$ is the single slot area, and

$l_{R,k}$ is the winding copper wire length of single phase. The mass of the motor is calculated below:

$$m_{mag,k} = b_{m,k} l_{m,k} l_k \rho_{mag}, \tag{33}$$

$$m_{steelr,k} = \pi \rho_{steel} l_k \left[\left(\frac{d_{2,k}}{2} - l_{m,k} \right) - \frac{d_{1,k}^2}{4} \right]^2 + 2 p_k m_{mag,k}, \tag{34}$$

$$t_{inter,k} = t_{1,k} + t_{2,k} + t_{4,k} + t_{5,k}, \tag{35}$$

$$m_{steel,k} = \rho_{steel,k} [\pi l_k (D_{1,k} + t_{inter,k}) t_{inter,k} - l_k S_{slot,k} z_k], \tag{36}$$

$$m_{copp,k} = 3\pi \left(\frac{d_k}{2} \right)^2 l_{R,k} \rho_{copp}, \tag{37}$$

$$m_{all,k} = m_{copp,k} + m_{steels,k} + m_{steel,k}. \tag{38}$$

Here, $m_{mag,k}$ represents the mass of a single magnetic steel, $m_{steelr,k}$ is the rotor mass, $m_{steel,k}$ is the stator steel mass, $m_{copp,k}$ is the mass of all the copper wire, and $m_{all,k}$ is the total motor mass. ρ_{steel} and ρ_{copp} are the density of the steel and the copper. d_k is the diameter of the copper wire. The motor rotor inertia is then presented below:

$$J_{rotor,k} = \frac{m_{steelr,k}}{2} \left(\frac{d_{1,k}^2 + d_{2,k}^2}{4} \right). \tag{39}$$

4 Optimization Design and Result Analysis

4.1 Cobot Optimization Strategy

To enhance the cobot's load capacity and increase flexibility in human-cobot interactions, this study focuses on designing the modular joint drive train to optimize the comprehensive performance of load capacity and dynamics. Constructing a comprehensive performance evaluation index poses a challenge, given the varying load capacity and dynamic parameters with changes in cobot pose. The attributes of these two indicators are inconsistent, leading to controversy in constructing the evaluation index.

To address this challenge, the proposed design method in this work adopts a multi-objective optimization approach. Two optimization indices are constructed independently, and the Pareto method is employed to determine the optimal design parameters.

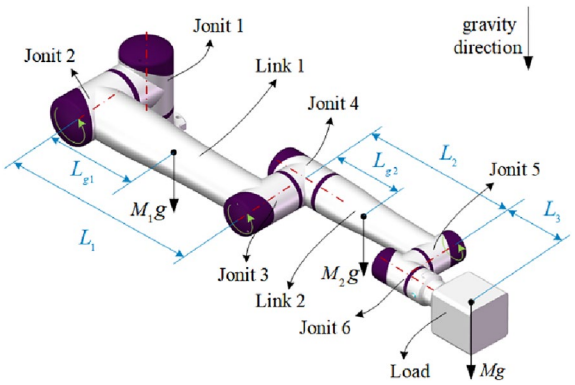

Figure 5 Six-axis cobot of the optimization case

Regarding the construction of optimization design indices, we formulate the indices when the robot is in a horizontal pose, which is shown in Figure 5, where the output force at the end effector of the robot is minimized. The optimization indices are outlined below.

4.1.1 Optimal Objective

Given the inter-joint load effects and the influence of the control algorithm on end effector dynamic characteristics, this study utilizes the minimum value of all joint resonance frequencies in the horizontal pose to formulate the dynamic performance function, as depicted in Eq. (41) Here, $\boldsymbol{\omega}$ represents the vector of joint resonance frequencies which is shown in Eq. (40), and $\min(\boldsymbol{\omega})$ is the minimum value within the vector. $\omega_{NTR,n}$ is the resonance frequency of the nth joint, and n is the number of the joints. Additionally, $\omega_{\max}$ and $\omega_{\min}$ represent the maximum and minimum values, respectively, of all $\min(\boldsymbol{\omega})$ set values, serving as the boundaries of the value range in the design domain. As the resonance frequency contains information of anti-resonance frequency, and the dynamic performance of the robot is related to the inertia of the motor axis, this work utilizes resonance frequency to construct optimization indices. In this work, the end effector mass is also a crucial factor for optimization, calculated as the nominal load in the industry divided by gravitational acceleration. Therefore, Eq. (41) normalizes the resonance frequency, where a larger $f_d(\boldsymbol{x})$ implies superior dynamic performance for a cobot. Here, $\boldsymbol{x}$ represents the vector of design variables, and $\boldsymbol{\omega}$ is the function of the vector $\boldsymbol{x}$.

$$\boldsymbol{\omega} = [\omega_{NTR,1}, \omega_{NTR,2}, \cdots, \omega_{NTR,n}], \tag{40}$$

$$f_d(\boldsymbol{x}) = \frac{\min(\boldsymbol{\omega}) - \omega_{\min}}{\omega_{\max} - \omega_{\min}}. \tag{41}$$

The load capacity performance function, $f_l(\boldsymbol{x})$ is presented in Eq. (42), where F_{uplift} represents the uplift force at the end effector, also being a function of vector $\boldsymbol{x}$. $F_{\max}$ and $F_{\min}$ denote the maximum and minimum values of F_{uplift} within the design domain, respectively. Equation (42) normalizes F_{uplift}, and a higher value of $f_l(\boldsymbol{x})$ indicates superior load capacity for a cobot.

$$f_l(\boldsymbol{x}) = \frac{F_{uplift} - F_{\min}}{F_{\max} - F_{\min}}. \tag{42}$$

Ensuring not only load capacity optimization but also the maximization of joint output torque is crucial. To achieve this, the joint motor's rated torque is calculated based on the reducer's maximum average load, and the rated speed is set accordingly. Employing a high torque density design approach for the motors reduces joint mass, thereby enhancing the cobot's load capacity [26, 27]. Consequently, for identical output torque and speed, the motor design can be determined by the air gap diameter [28] as the high torque density design approach of motor makes that only one variable is allowed between length and diameter.

In this study, the outer diameter of the motor rotor is selected as the optimal design variable. Hence, vector **x** is a function of each joint motor rotor outer diameter and the joint reduction ratios, as illustrated in Eq. (43):

$$\boldsymbol{x} = f(d_{2,1}, d_{2,2}, \cdots, d_{2,n}, N_1, N_2, \cdots, N_n). \tag{43}$$

4.1.2 Constraints

All the formulas from Eqs. (1) to (39) represent constraints, encompassing joint dynamics and the motor design process. Additional constraints are outlined in Eq. (44), where $[d_{2,k\,\min}, d_{2,k\,\max}]$ defines the range for the kth joint motor rotor outer diameter. $\{N_{1,k}, N_{2,k}, \cdots, N_{y,k}\}$ signifies the reduction ratio vector of the kth joint, where y is the number of reduction ratios. $\boldsymbol{M}(\boldsymbol{q})_{(k,k)}$ denotes the inertia of the cobot converted to the kth joint. K_k represents the stiffness of the kth joint, constituting the kth parameter of the stiffness vector $\boldsymbol{K}_{(k)}$. n is the total number of joints.

$$s.t.\begin{cases} d_{2,k} \in [d_{2,k\min}, d_{2,k\max}] \\ N_k \in \{N_{1,k}, N_{2,k}, \cdots, N_{y,k}\} \\ J_{l,k} = \mathbf{M}(\mathbf{q})_{(k,k)} \\ K_k = \mathbf{K}_{(k)} \\ k = 1, 2, \cdots n \end{cases} \tag{44}$$

4.1.3 Optimization Strategy

The enumeration method is employed for optimizing the objective function, mitigating the risk of being trapped in local optima and simplifying the analysis of the design process. Given the computational intensity of motor design, discretizing the motor design scheme proves beneficial to enhance the optimization design speed. The specific optimization steps are as follows:

Step 1: Establish the configuration and dimensions of the links. Additionally, identify the type of harmonic reducer and input its parameters, encompassing mass, wave generator rotational inertia, sets of reduction ratios, stiffness, rated load, and speed.

Step 2: Preliminarily determine the size of the joint structure. Design the motor considering the constraints of joint size, the rated load, and speed of the reducer, establishing the design range for the motor. Discretize the design range for the motor rotor's outer diameter.

Step 3: Employ the enumeration method to compute $\omega_{\max}$ and $\omega_{\min}$, $F_{\min}$, and $F_{\max}$ adhering to the constraints specified in Eq. (44).

Step 4: Calculate $f_d(\boldsymbol{x})$ and $f_l(\boldsymbol{x})$ using the enumeration method, and ascertain the optimal design scheme by analyzing the Pareto front.

4.2 Optimization Case

4.2.1 Preliminary Design

The optimization design method is employed to design a six-axis cobot, as illustrated in Figure 5. The configuration of the six-axis cobot is depicted in Figure 1(b), with the fourth joint positioned close to the third joint to enhance the cobot's load capacity. Considering factors such as product appearance design, manufacturing, and comparison with commercial cobot, this cobot is equipped with only three types of joints. Specifically, joint 1, joint 3, and joint 5 are identical, while joint 2, joint 4, and joint 6 share similarities, with slight offsets introduced in joint 6 to simplify the machining process. Therefore, in the worst-case scenario pose, the optimization design of joint 2, joint 3, and joint 5 becomes critical in the cobot's design.

Building on the aforementioned analysis, the preliminary design and 3D modeling of the cobot are conducted, with a benchmark against a 5 kg load capacity industrial cobot. The density and dimensional parameters closely approximate those of the real prototype, ensuring that the physical parameters are accurate enough for the design optimization.

Joint 1 and joint 2 are fitted with the HSG-25 reducer model, while joint 3 and joint 4 utilize the HSG-20 reducer model. Joint 5 and joint 6 are equipped with the HSG-14 reducer model.

Table 1 Parameters of the six-axis cobot

Parameters	Value	Parameters	Value
L_1	524 mm	$M_{j,2}$	3.3 kg
L_2	407 mm	$M_{j,3}$	2.1 kg
L_3	100 mm	$M_{j,4}$	2.1 kg
L_{g1}	283 mm	$M_{j,5}$	1.1 kg
L_{g2}	215 mm	$M_{j,6}$	1.1 kg
M	5 kg	$J_{wg,2}$	0.42 kg·cm^2
M_1	1.6 kg	$J_{wg,3}$	0.16 kg·cm^2
M_2	0.7 kg	$J_{wg,5}$	0.11 kg·cm^2
$M_{j,1}$	3.3 kg		

The initial parameters are presented in Table 1. Here, L_1 signifies the length of Link 1, while L_2 represents the length of Link 2. Additionally, L_3 indicates the distance from the axis of joint 5 to the center of mass of the end effector. L_{g1} and L_{g2} correspond to the distances from the axes of joints 1 and 3 to the centers of mass of Links 1 and 2, respectively. M is the mass of the end effector, serving as a reference for the 5 kg load capacity of a commercial cobot. Furthermore, M_1 and M_2 denote the mass values of Link 1 and Link 2, respectively. g is the gravitational acceleration. Lastly, $M_{j,1}$ represents the mass value of the kth joint component, excluding the joint rotation shaft components, while $J_{wg,k}$ signifies the rotational inertia of the wave generator of the kth joint harmonic reducer.

4.2.2 Setup of the Boundary

The initial joint design establishes the parameters for motor design, as expressed in Eq. (45). These constraints encompass the range of the motor rotor's inner diameter, the motor stator's outer diameter, the motor length, the reducer's rated torque, the motor's rated velocity, and the high-torque -density design approach for the motor.

$$\text{s.t.,} \begin{cases} 30 \le d_{1,2} \le D_{2,2} \le 88, \\ 22 \le d_{1,3} \le D_{2.3} \le 70, \\ 16 \le d_{1,5} \le D_{2,5} \le 50, \\ l_2 \in (0,50],\ l_3 \in (0,50],\ l_5 \in (0,50], \\ \tau_{mc,2} = 140,\ \tau_{mc,3} = 64,\ \tau_{mc,5} = 12, \\ \dot{\theta}_2 = \dot{\theta}_3 = \dot{\theta}_5 = 314. \end{cases} \tag{45}$$

The viable motor design space is investigated by adhering to the constraints outlined in Eq. (45), and the resultant feasible design options are illustrated in Figure 6. The design of these motors emphasizes high torque density, entailing the imposition of various constraints throughout the design procedure. Key factors influencing the motor specifications include the rated torque, rated speed, and distinctive dimensions.

In this investigation, the chosen dimension variable is the motor rotor outer diameter ($d_{2,k}$), with the rated torque and rated speed being determined by the rated parameters of the reducer. Figure 6(a), (b) and (c) illustrate the motor design spaces for joint 2, corresponding to reducer reduction ratios of 80, 100, and 120. Likewise, (d), (e) and (f) display the motor design spaces for joint 3, featuring reducer reduction ratios of 50, 80, and 100, while (g), (h) and (i) showcase the motor design spaces for joint 5, with reducer reduction ratios of 50, 80, and 100. Figure 6 graphically represents the motor mass and the rotational inertia of the motor rotor.

The findings from Figure 6 reveal a positive correlation between the motor rotor's rotational inertia and outer diameter, while motor length and mass decrease with an increase in rotor outer diameter when the output torque and speed are constants. Constraints for motor diameter are outlined in Eq. (46), defining the limitations for optimal functions. Specifically, the range for $d_{2,2}$ is from 44 mm to 58 mm, for $d_{2,3}$ it's from 32 mm to 42 mm, and for $d_{2,5}$ it's from 24 mm to 32 mm. Here, N_2, N_3, and N_5 denote the reducer's reduction ratios.

In this study, the stiffness value of the harmonic reducer is chosen from the middle section of the time varying stiffness, aligning with real industrial applications. The motor design process and the preliminary cobot design also serve as key components of the boundary conditions for the optimized design.

$$\text{s.t.,} \begin{cases} 44 \text{ mm} \le d_{2,2} \le 58 \text{ mm}, \\ 32 \text{ mm} \le d_{2,3} \le 42 \text{ mm}, \\ 24 \text{ mm} \le d_{2,5} \le 30 \text{ mm}, \\ N_2 \in \{80, 100, 120\}, \\ N_3 \in \{50, 80, 100\}, \\ N_5 \in \{50, 80, 100\}, \\ K_2 = 50000\ ,\ K_3 = 25000\ ,\ K_5 = 6100. \end{cases} \tag{46}$$

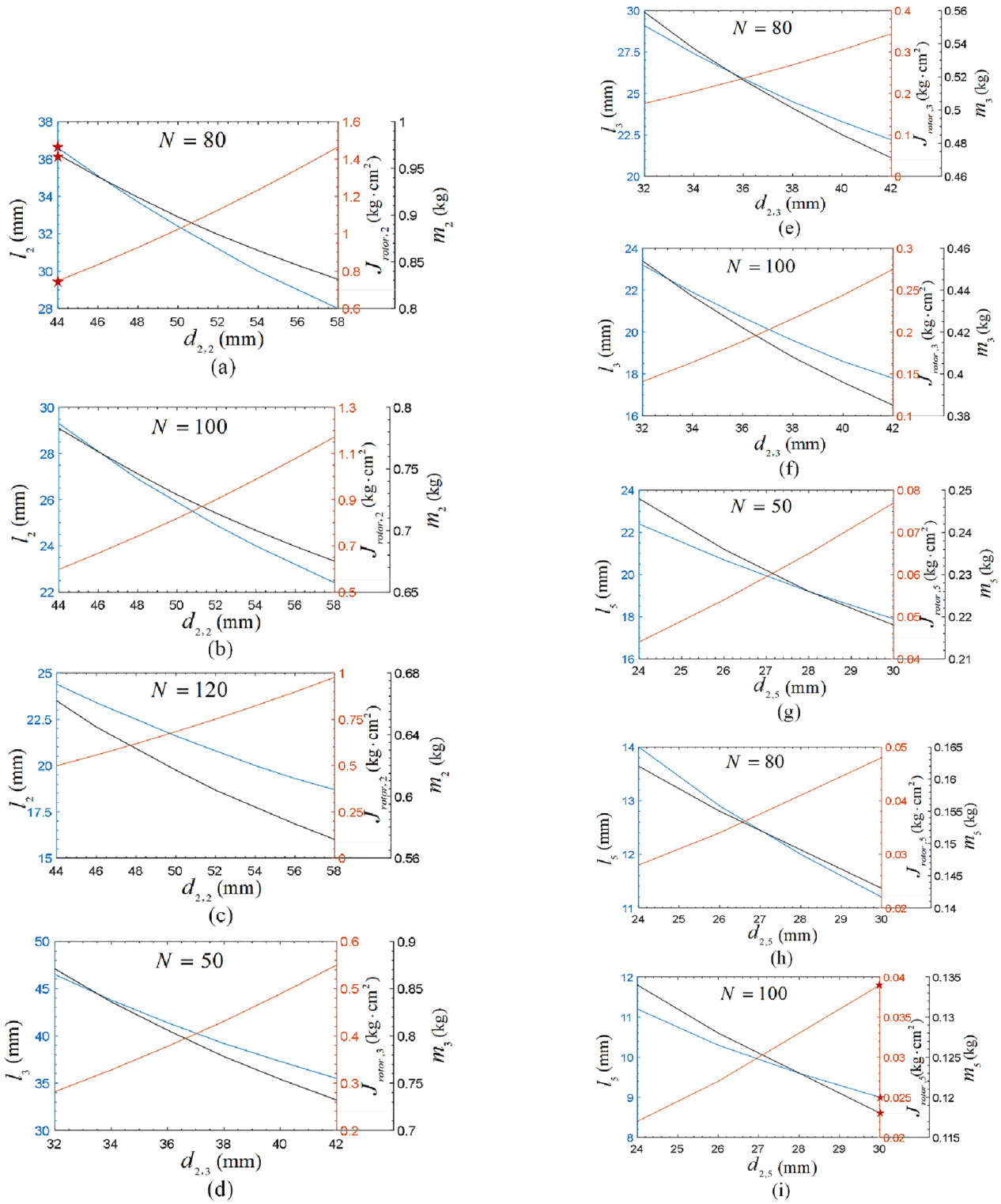

Figure 6 Motor design domains of the joint 2, 3 and 5: (**a**) The design spaces of joint 2 with *N*=80, (**b**) The design spaces of joint 2 with *N*=100, (**c**) The design spaces of joint 2 with *N*=120, (**d**) The design spaces of joint 3 with *N*=50, (**e**) The design spaces of joint 3 with *N*=80, (**f**) The design spaces of joint 3 with *N*=100, (**g**) The design spaces of joint 5 with *N*=50, (**h**) The design spaces of joint 5 with *N*=80, (**i**) The design spaces of joint 5 with *N*=100

4.2.3 Optimization Process

The discretization of the motor design feasible solution can significantly enhance calculation speed. To achieve this, the variable $d_{2,k}$ is discretized with engineering precision. The discrete set for $d_{2,2}$ includes {44, 46, 48, 50, 52, 54, 56, 58}, $d_{2,3}$ includes {32, 34, 36, 38, 40, 42}, and $d_{2,5}$ includes {24, 26, 28, 30}. Consequently, there are a total of 5184 design solutions to be considered, accounting for the reduction ratio. The enumeration method is employed to identify the optimal solution, aiding in avoiding issues related to local optimality. The steps for this process are as follows.

Algorithm Enumeration

Input:
The variables $d_{2,2}$, $d_{2,3}$, $d_{2,5}$, N_2, N_3, N_5, K_2, K_3, K_5;
The performance functions $f_d(\mathbf{x})$ and $f_l(\mathbf{x})$;
Output:

```
for N2 =80, 100, 120;
  for d2,2 =44, 46, ⋯ , 58;
    for N3 =50, 80, 100;
      for d2,3 =32, 34, ⋯ , 42;
        for N5 =50, 80, 100
          for d2,5 =24, 26, ⋯ , 30;
          Calculate ωmax , ωmin , Fmin , Fmax
          end for
        end for
      end for
    end for
  end for
for N2 =80, 100, 120;
  for d2,2 =44, 46, ⋯ , 58;
    for N3 =50, 80, 100;
      for d2,3 =32, 34, ⋯ , 42;
        for N5 =50, 80, 100
          for d2,5 =24, 26, ⋯ , 30;
            Calculate fd(x) and fl(x);
          end for
        end for
      end for
    end for
  end for
Return all the values of fd(x) and fl(x);
```

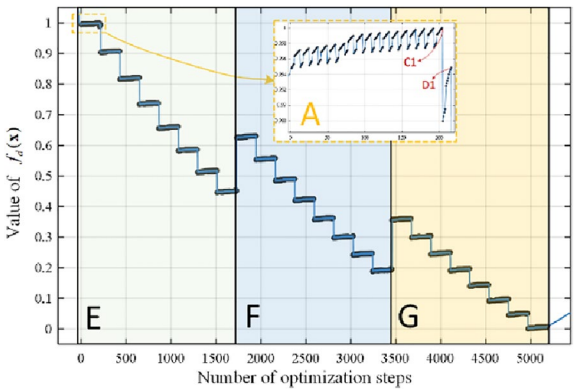

Figure 7 Values distribution of the objective $f_d(\boldsymbol{x})$ in the optimization process

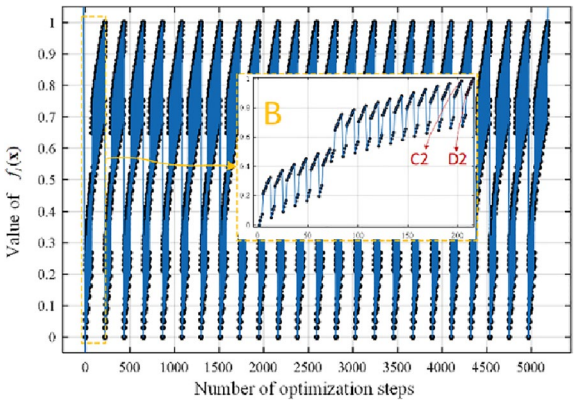

Figure 8 Values distribution of the objective $f_l(\boldsymbol{x})$ in the optimization process

4.2.4 Optimal Solution

The calculations indicate that $\omega_{\min}$ is 27.55 Hz and $\omega_{\max}$ is 42.78 Hz occurring at the 4969th and the 204th steps, respectively. $F_{\min}$ is 75.17 N and $F_{\max}$ is 82.56 N appearing at multiple steps, indicating the presence of several optimal solutions. All the data of $f_d(\boldsymbol{x})$ and $f_l(\boldsymbol{x})$ are plotted in Figures 7 and 8.

The data presented in Figures 7 and 8 illustrate the presence of local optimal solutions for the function $f_d(\boldsymbol{x})$ and the periodicity of the function $f_l(\boldsymbol{x})$. This observation suggests that the enumeration method is suitable for finding the global optimal solution for the drivetrain design. The maximum values of functions $f_d(\boldsymbol{x})$ and $f_l(\boldsymbol{x})$ occur before the 216th step in the process, with a focus on sections A and B during the analysis.

In section B, the data shows a growth trend in the form of bands. However, in section A, the data exhibits an increasing trend, except for the last band, which shows a downward trend. Consequently, the maximum values of the functions $f_d(\boldsymbol{x})$ and $f_l(\boldsymbol{x})$ do not coincide at the same

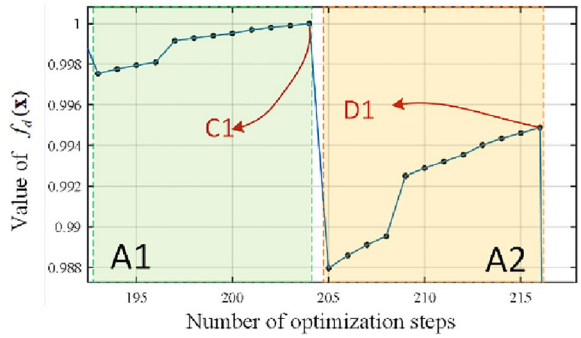

Figure 9 The last two bands of the section A

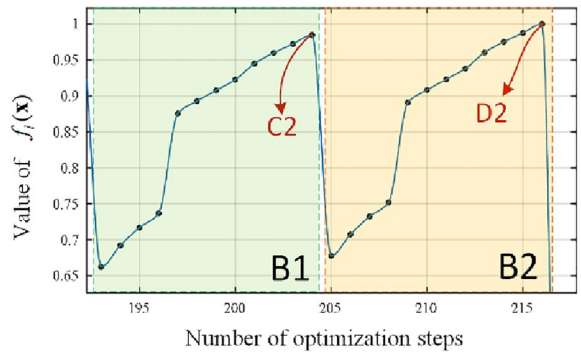

Figure 10 The last two bands of the section B

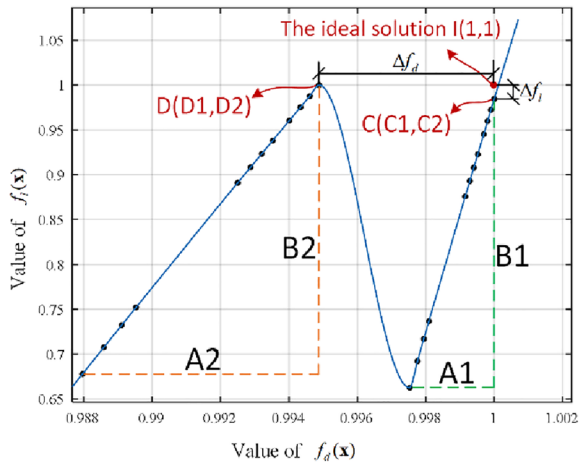

Figure 11 The Pareto front of the optimization

optimization point. The last two bands in sections A and B are specifically focused on and plotted in Figures 9 and 10.

In Figures 9 and 10, C1 and C2 correspond to the 204th step of the optimization process, representing the optimal values of bands A1 and B1. Similarly, D1 and D2 correspond to the 216th step, signifying the optimal values of bands A2 and B2. However, the condition that C1 is larger than C2 and D1 is less than D2 introduces uncertainty regarding the global optimal value. To address this, the Pareto front is plotted in Figure 11 using data from A1, A2, B1 and B2 to obtain the global optimal value.

Table 2 Result of the optimization

Variable	Value	Variable	Value
N_2	80	$m_{all,2}$	0.965 kg
N_3	100	$m_{all,3}$	0.385 kg
N_5	100	$m_{all,5}$	0.118 kg
$d_{2,2}$	44 mm	$J_{rotor,2}$	0.748 kg·cm^2
$d_{2,3}$	42 mm	$J_{rotor,3}$	0.275 kg·cm^2
$d_{2,5}$	30 mm	$J_{rotor,5}$	0.039 kg·cm^2

The horizontal axis represents $f_d(\boldsymbol{x})$, while the vertical axis represents $f_l(\boldsymbol{x})$ in Figure 11. The ideal solution is represented by point I, indicating that functions $f_d(\boldsymbol{x})$ and $f_l(\boldsymbol{x})$ simultaneously achieve their optimum values. Therefore, the distance from the function values to point I(1,1) serves as a metric to evaluate the optimality of each design scheme, with the optimum design achieved when this distance is minimized. Intuitively, the optimum is reached at either C(C1, C2) or D(D1, D2), and the distance is calculated using Eqs. (47) and (48):

$$\Delta f_d = |\mathrm{ID}| = 0.0052, \tag{47}$$

$$\Delta f_l = |\mathrm{IC}| = 0.0153. \tag{48}$$

As $\Delta f_d < \Delta f_l$, it indicates that point D is the global optimum, which is reached at the 216th step, and the corresponding design results are shown in Table 2.

4.3 Optimization Result Analysis

The design results indicate that the payload capacity of the cobot has reached the global maximum, and the optimization function for the dynamic performance of the cobot is also close to its maximum value. During the optimization process, due to the discrete nature of the speed ratio selection of the deceleration mechanism and the use of an enumeration method for optimization, the overall presentation shows discrete band characteristics, and there are local optimal solutions. In Figure 7, the three regions E, F, and G correspond to the speed ratios of joint 2 in the optimization process, namely 80, 100, and 120. The starting segment of region F is higher than the ending segment of region E, and similarly, the starting segment of region G is higher than the ending segment of region F. The starting segment of region E is identified as the globally optimal segment.

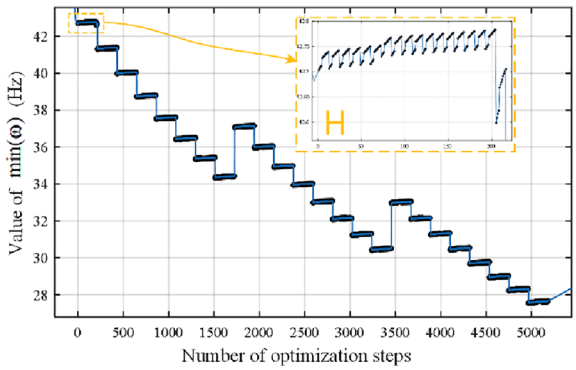

Figure 12 Values distribution of min($\boldsymbol{\omega}$) in the optimization process

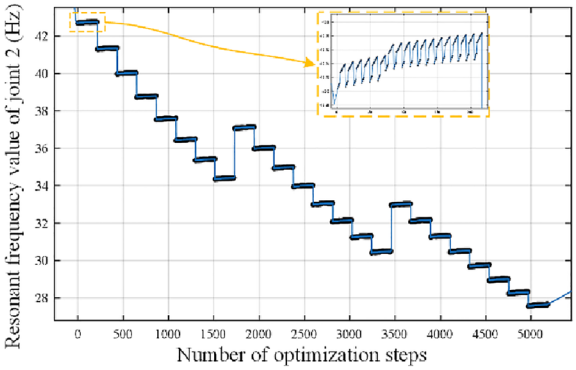

Figure 13 Values distribution of the joint 2 resonance frequency in the optimization process

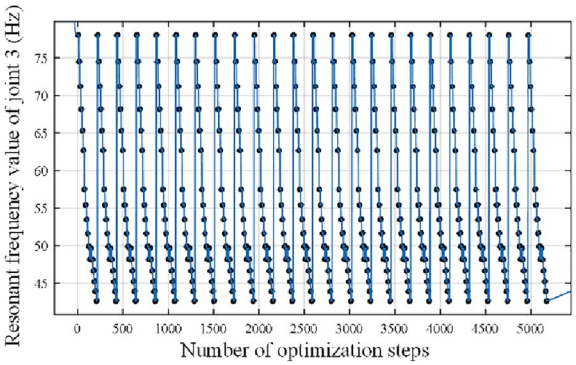

Figure 14 Values distribution of the joint 3 resonance frequency value in the optimization process

The optimized results show that the reducer's reduction ratio selected for joint 2 is the largest in the set. The corresponding motor resulting from optimization has a relatively large length-to-diameter ratio, larger mass, and small rotor rotational inertia. For joints 3 and 5, the reducers' reduction ratio is the largest in the set. The motor selected through optimization has a small mass and a larger shaft rotational inertia. The motor design results are indicated by the red stars in Figure 6.

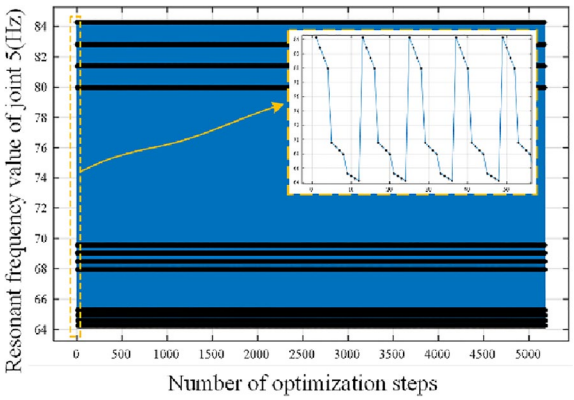

Figure 15 Values distribution of the joint 5 resonance frequency value in the optimization process

Figure 12 displays a distribution plot of min($\boldsymbol{\omega}$), demonstrating a similar partition trend to the function $f_d(\boldsymbol{x})$. However, its vertical axis represents the actual values of min($\boldsymbol{\omega}$). The maximum value of min($\boldsymbol{\omega}$) is 42.78 Hz, and the minimum value is 27.55 Hz.

The resonance frequency of each joint is crucial for the overall dynamic characteristics of cobot. Therefore, the distribution of resonance frequencies for the joint 2, 3, 5 of the cobot is studied in the design state during the optimization process, as shown in Figures 13, 14, 15.

Figure 13 illustrates that the maximum resonance frequency of joint 2 is 42.78 Hz at the 216th step, while the minimum resonance frequency is 27.55 Hz at the 4969th step. Moving to Figure 14, it presents the data of joint 3 resonance frequency, with the maximum value reaching 78.09 Hz at the first point of each band and the minimum value 42.60 Hz at the 205th step. The 216th step value is 42.70 Hz which is the optimization result. Similarly, Figure 15 provides data for joint 5 resonance frequency, where the maximum value is 84.28 Hz at the first point of each band and the minimum value is 64.24 Hz at the last point of each band. Consequently, the last band in section H of Figure 12 represents data for joint 3, while the remaining data corresponds to joint 2.

Analyzing diagrams 13, 14, and 15, we can observe that the resonance frequency of joint 3 is almost entirely higher than that of joint 2. Additionally, for joint 5, its resonance frequency is mostly higher than that of joint 3. Therefore, for cobot, joints closer to the base have the most significant impact on the overall dynamic performance of the cobot. The optimal joint drive train scheme is achieved at step 216th, where the resonance frequency of joint 2 is at its maximum, while the resonance frequencies of joints 3 and 5 are at their minimum.

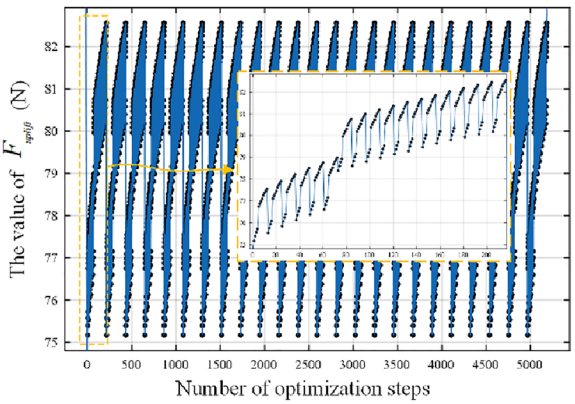

Figure 16 Values distribution of F_{uplift} in the optimization process

Figure 16 is the value of the cobot lifting force. It can be observed that the cobot's maximum lifting force is 82.56 N, and the minimum lifting force is 75.17 N. The maximum value is achieved at the 216th step of the optimization process. The maximum value is 10% greater than the minimum value.

The optimized results indicate that successfully improving the cobot's load capacity is achieved by reducing the mass of joints 3 to 6. This reduction enables the joints to exert greater external force while simultaneously increasing the resonance frequencies of joints 2 and 1, thereby enhancing the cobot's dynamic response performance.

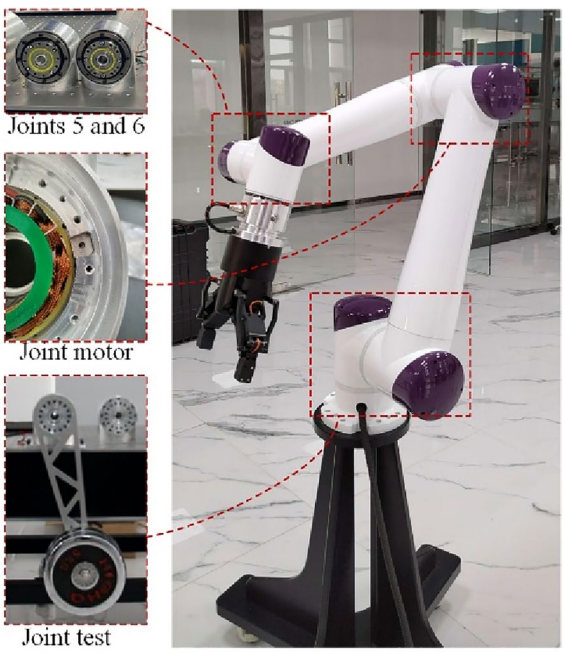

Figure 17 The prototype of cobot design case

Table 3 Parameter Comparison table of relevant benchmark commercial robots

Model	Payload (kg)	Self-weight (kg)	Working radius (mm)
UR5e	5	18.4	850
AUBO-i5	5	24	886.5
Design case	8.4	19.9	1031

Considering that the resonance frequency distribution band of joint 2 is the lowest among joints 2, 3 and 5, the optimization design process selects a scheme for joint 2 with the maximum resonance frequency. However, this choice involves a trade-off, as it sacrifices the optimal resonance frequencies of joints 3 and 5 to enhance the cobot's load capacity. Based on the optimized design results, a cobot prototype is produced and shown in Figure 17.

To effectively demonstrate the effect of the optimized design, this study compares its results with the parameters of commercial cobot, as listed in Table 3.

Due to the unavailability of dynamic characteristic parameters for commercial cobot, the comparison in this study is limited to load capacity, self-weight and working radius parameters, which are used to illustrate the cobot load performance. Given that the design case in this study aligns with commercial 5 kg payload cobot, a comparison is conducted with UR5e [29] and AUBO-i5 [30]. From Table 3, it can be seen that the design case has the maximum payload, and the largest working radius. Therefore, the cobot's load capacity in the design case is superior, indicating the effectiveness of the design.

5 Conclusions

The lightweight structural design results in a relatively lower load capacity for the cobot. Simultaneously, enhancing the dynamic response characteristics of cobot is crucial for improving human-robot collaboration performance. Therefore, this study focuses on optimizing the overall performance of the cobot in terms of load capacity and dynamic response characteristics through the design of the joint transmission system. The conclusions are summarized as follows:

(1) Using joint resonance frequency and cobot load capacity to construct optimization indicators, and applying the Pareto frontier to optimize the joint transmission system, can achieve the optimal comprehensive performance of cobot's dynamic response and load capacity.
(2) The design process reveals that joints near the base have the lowest resonance frequency design domain. Therefore, it is necessary to concentrate on

designing the drive train for these joints to enhance the cobot's dynamic response characteristics. The design results indicate that joints near the base are best suited for the adoption of harmonic reducers with a small reduction ratio and motors with low rotor inertia, which helps improve the cobot's dynamic response characteristics.

(3) For joints far from the base, their drive train need to adopt harmonic reducers with a large reduction ratio and lightweight motors to enhance the cobot's load capacity.

(4) Compared to commercial cobot, the cobot in this design case has higher load capacity.

Based on the analysis above, the method proposed in this work can enable cobot to achieve optimal integration of load and dynamic response characteristics. This method is versatile, applicable not only to six-axis collaborative robots but also suitable for designing seven-axis collaborative robots and other electromechanical devices

Acknowledgements
The authors sincerely thanks to Professor Chin-Yin Chen of Ningbo Institute of Materials Technology and Engineering, Chinese Academy of Sciences for his discussion and reading during manuscript preparation.

Authors' Contributions
PL wrote the manuscript and made the prototype. ZN checked and improved the manuscript in writing. All authors read and approved the final manuscript.

Funding
Supported by National Key Research and Development Program of China (Grant Nos. 2022YFB4703000, 2019YFB1309900).

Declarations

Competing Interests
The authors declare no competing financial interests.

Received: 19 November 2023 Revised: 22 April 2024 Accepted: 10 May 2024
Published online: 12 June 2024

References

[1] E Matheson, R Minto, E G G Zampieri, et al. Human-robot collaboration in manufacturing applications: A review. *Robotics*, 2019, 8(4): 100.
[2] L Wang, R Gao, J Váncza, et al. Symbiotic human-robot collaborative assembly. *CIRP Annals*, 2019, 68(2): 701-726.
[3] M Faccio, M Bottin, G Rosati. Collaborative and traditional robotic assembly: A comparison model. *The International Journal of Advanced Manufacturing Technology*, 2019, 102: 1355-1372.
[4] L Zhou, S Bai, M R Hansen. Integrated dimensional and drive-train design optimization of a light-weight anthropomorphic arm. *Robotics and Autonomous Systems*, 2012, 60(1): 113-122.
[5] L Zhou, S Bai, M R Hansen. Design optimization on the drive train of a light-weight robotic arm. *Mechatronics*, 2011, 21(3): 560-569.
[6] L Zhou, S Bai. A new approach to design of a lightweight anthropomorphic arm for service applications. *ASME Journal of Mechanisms and Robotics*, 2015, 7(3): 031001.
[7] H Yin, J Liu, F Yang. Hybrid structure design of lightweight robotic arms based on carbon fiber reinforced plastic and aluminum alloy. *IEEE Access*, 2019, 7: 64932-64945.
[8] Prachi V Karlekar, Swapna Choudhary, Atul Deshmukh, et al. Innovations in urban automation: Robotic arm integration in smart city environments. *2023 International Conference on Sustainable Emerging Innovations in Engineering and Technology (ICSEIET)*, Ghaziabad, India, 2023: 314-319.
[9] H Yin, C Kong, M He, et al. Double-parameter regression design of drive trains for lightweight robotic arms. *ASIAN MMS CCMMS*, Singapore, 16 November 2016, 408: 223-236.
[10] J Li, J Liu, Y Hu, et al. Integrated optimization for service robotic arms involving workspace, drive train, structural stiffness and lightweight. *2021 5th International Conference on Robotics and Automation Sciences (ICRAS)*, Wuhan, China, 2021: 44-50.
[11] K Kawaharazuka, T Makabe, K Okada, et al. Daily assistive modular robot design based on multi-objective black-box optimization. *2023 IEEE/RSJ International Conference on Intelligent Robots and Systems (IROS)*, 2023: 9970-9977.
[12] W He, P Zhang, K Guo, et al. Kinematic calibration and compensation of industrial robots based on extended joint space. *IEEE Access*, 2023, 11: 109331-109340.
[13] E A Padilla-Garcia, A Rodriguez-Angeles, J R Reséndiz, et al. Concurrent optimization for selection and control of AC servomotors on the powertrain of industrial robots. *IEEE Access*, 2018, 6: 27923-27938.
[14] R Citalán-Lara, C A Cruz-Villar. Multidisciplinary optimization of servodrives for robot manipulators. *2014 IEEE/ASME International Conference on Advanced Intelligent Mechatronics*, Besacon, France, 2014: 38-43.
[15] H Song, Y S Kim, J Yoon, et al. Development of low-inertia high-stiffness manipulator LIMS2 for high-speed manipulation of foldable objects. *2018 IEEE/RSJ International Conference on Intelligent Robots and Systems (IROS)*, Madrid, Spain, 2018: 4145-4151.
[16] Z Du, Y Xiao, W Dong. Method for optimizing manipulator's geometrical parameters and selecting reducers. *Journal of Central South University*, 2013: 1235-1244.
[17] T Çallar, S Böttger. Hybrid learning of time-series inverse dynamics models for locally isotropic robot motion. *IEEE Robotics and Automation Letters*, 2023, 8(2): 1061-1068.
[18] G Hirzinger, N Sporer, M Schell, et al. Torque-controlled light weight arms and articulated hands — Do we reach technological limits now? *Springer Tracts in Advanced Robotics*, 2003, 5: 21-47.
[19] M Iskandar, C Ott, O Eiberger, et al. Joint-level control of the DLR lightweight robot SARA. DLR [2023-11-17]. https://www.dlr.de/rm/en/desktopdefault.aspx/tabid-11709/#gallery/29681.
[20] T Asfour, M Waechter, L Kaul, et al. ARMAR-6: A high-performance humanoid for human-robot collaboration in real-world scenarios. *IEEE Robotics & Automation Magazine*, 2019, 26(4): 108-121.
[21] D Shah, M Savoldi, A Scalzo, et al. Towards design and development of new joint modules for humanoid ergoCub 2.0*. *2023 IEEE-RAS 22nd International Conference on Humanoid Robots (Humanoids)*, Austin, TX, USA, 2023: 1-7.
[22] C Lv, G Chen, H Zhao, et al. An adaptive robust hybrid force/position control for robot manipulators system subject to mismatched and matched disturbances. *IEEE Access*, 2024, 12: 42264-42278.
[23] C Ren, H Jiang, C Mu, et al. Conditional disturbance negation based control for an omnidirectional mobile robot: An energy perspective. *IEEE Robotics and Automation Letters*, 2022, 7(4): 11641-11648.
[24] J Song, E Chu, D Yang, et al. Novel SVPWM method based on zero-voltage notch of resonant DC-link inverter. *IEEE Transactions on Power Electronics*, 2023, 38(7): 8544-8558.
[25] P Guo, Y Li, Z Lin, et al. Characterization and calculation of losses in soft magnetic composites for motors with SVPWM excitation. *Applied Energy*, 2023, 349: 121631.
[26] Y Zhang, D Li, L Fang, et al. Design and manufacture of a high-torque-density permanent magnet traction motor for light-duty electric vehicles. *IEEE Transactions on Transportation Electrification*, 2024, 10(1): 379-391.
[27] Z Xiang, S Bi, X Zhu, et al. High torque density and lightweight design of permanent magnet in-wheel motor based on magnetic field modulation effect. *IEEE Transactions on Magnetics*, 2023, 59(11): 1-7.
[28] S Park, J Park, J Kim, et al. Design of high bandwidth motor system considering electrical and mechanical time constants. *2019 IEEE Energy*

Conversion Congress and Exposition (ECCE), Baltimore, MD, USA, 2019: 3110-3116.
[29] The reference manual of cobot UR5e. UR, [2023-11-17]. https://www.universal-robots.com/products/ur5-robot/.
[30] The production parameter of AUBO-i5. AUBO, [2023-11-17]. https://www.aubo-cobot.com/public/products3

Peng Li born in 1989, is currently a PhD candidate at *Department of Mechanical Engineering, Tsinghua University, China*. His research interests include mechatronic system, robotics, torque sensor, motor, encoder and compliance control.

Zhenguo Nie born in 1983, is currently an assistant professor at *Department of Mechanical Engineering, Tsinghua University, China*. His research interests include the intersection of intelligent robots and medical workers: cobot, medical robots, and intelligent orthopedic devices.

Zihao Li born in 1992, is currently a PhD candidate at *Department of Mechanical Engineering, Tsinghua University, China*. His research interests include teleoperation, human-robot interaction and compliance control.

Xinjun Liu is currently a professor and a PhD candidate supervisor at *Department of Mechanical Engineering, Tsinghua University, China*. His research interests include robotics, parallel mechanisms, and advanced manufacturing equipment.